ISPRS Journal of Photogrammetry and Remote Sensing 109 (2015) 98–107

Contents lists available at ScienceDirect

ISPRS Journal of Photogrammetry and Remote Sensing

journal homepage: www.elsevier.com/locate/isprsjprs

A Synergy Method to Improve Ensemble Weather Predictions and Differential SAR Interferograms

Franz-Georg Ulmer *, Nico Adam

Deutsches Zentrum für Luft- und Raumfahrt (DLR), Institut für Methodik der Fernerkundung, Münchener Straße 20, 82234 Weßling, Germany

ARTICLE INFO

Article history:
Received 19 March 2015
Received in revised form 11 August 2015
Accepted 15 September 2015

Keywords:
APS
NWP
DInSAR
PSI
Atmosphere mitigation
Pressure hindcast

ABSTRACT

A compensation of atmospheric effects is essential for mm-sensitivity in differential interferometric synthetic aperture radar (**DInSAR**) techniques. Numerical weather predictions are used to compensate these disturbances allowing a reduction in the number of required radar scenes. Practically, predictions are solutions of partial differential equations which never can be precise due to model or initialisation uncertainties. In order to deal with the chaotic nature of the solutions, ensembles of predictions are computed. From a stochastic point of view, the ensemble mean is the expected prediction, if all ensemble members are equally likely. This corresponds to the typical assumption that all ensemble members are physically correct solutions of the set of partial differential equations. DInSAR allows adding to this knowledge. Observations of refractivity can now be utilised to check the likelihood of a solution and to weight the respective ensemble member to estimate a better expected prediction.

The objective of the paper is to show the synergy between ensemble weather predictions and differential interferometric atmospheric correction. We demonstrate a new method first to compensate better for the atmospheric effect in DInSAR and second to estimate an improved numerical weather prediction (**NWP**) ensemble mean. Practically, a least squares fit of predicted atmospheric effects with respect to a differential interferogram is computed. The coefficients of this fit are interpreted as likelihoods and used as weights for the weighted ensemble mean. Finally, the derived weighted prediction has minimal expected quadratic errors which is a better solution compared to the straightforward best-fitting ensemble member. Furthermore, we propose an extension of the algorithm which avoids the systematic bias caused by deformations. It makes this technique suitable for time series analysis, e.g. persistent scatterer interferometry (**PSI**). We validate the algorithm using the well known Netherlands-DInSAR test case and first show that the atmospheric compensation improves by nearly 40% compared to the straightforward technique. Second, we compare our results with independent sea level pressure data. In our test case, the mean squared error is reduced by 29% compared to the averaged ensemble members with equal weights. An application demonstration using actual Sentinel-1 data and a typical test site with significant subsidence (Mexico City) completes the paper.

1. Introduction

Synthetic aperture radar (**SAR**) is a popular remote sensing technique to observe the topography of the earth and its millimetre displacements. The strength of a signal which is scattered back is independent of the actual weather condition. However, the wave propagation velocity depends on water vapour, pressure and temperature (see Smith and Weintraub, 1953).

Differential interferometric synthetic aperture radar (**DInSAR**) images are subtracted phase information of two SAR acquisitions, corrected for topography, and are therefore affected by atmosphere. In order to allow precise interferometric measurements, the atmospheric effect needs to be compensated and is known as atmospheric phase screen (**APS**). Currently, the time series analysis using large stacks of SAR data is well established. Essentially, it is based on the uncorrelated atmosphere with respect to time requiring a long time series (see Ferretti et al., 2001). Different authors have successfully demonstrated the mitigation of the APS using NWP, for example (Holley et al., 2007; Jung et al., 2014; Nico et al., 2011; Adam, 2013; Pierdicca et al., 2011; Perissin et al.,

* Corresponding author.
E-mail addresses: Franz-Georg.Ulmer@dlr.de (F.-G. Ulmer), Nico.Adam@dlr.de (N. Adam).

http://dx.doi.org/10.1016/j.isprsjprs.2015.09.004
0924-2716/

2011). These papers show that the hydrostatic component can be estimated using NWP models. However in practice, the wet-delay is more difficult to reproduce using numerical weather prediction (**NWP**) due to its turbulent nature. For the second application, i.e. improved numerical weather prediction (Pichelli et al., 2015) have demonstrated a better forecast for weak to moderate precipitation.

NWP implements a set of partial differential equations (**PDEs**). The solution can never be precise due to model or initialisation uncertainties. In practice, the initial atmosphere state data are spatially undersampled and affected by measurement errors. Additionally, different options (e.g. resolution, size of simulated area, physics options and integration time step length) result in different valid (i.e. physically correct) solutions of the PDEs (Liu et al., 2011). Another effect results from error propagation. Imprecise convection strength causes timing deviations. As a result, humidity is dislocated with time of day.

Epstein (1969) proposed a stochastic dynamic model (i.e. ensembles of PDEs solutions) to handle uncertainties produced by the weather prediction model or the initialisation data. An ensemble represents likely atmospheric states and it spreads the uncertainties. It is a well established practice to use independent atmosphere state observations e.g. sounding, lidar and weather stations. Hence, ensemble members can be verified by such observations. A straightforward approach is to use only the most likely (best fitting) ensemble member. Another method linearly combines the ensemble members. The second tactic allows a better fit of the prediction to the practically observed data. However, this improvement can only be ensured at the measurement location. In other areas, over-fitting can occur. We demonstrate the use of DInSAR data as independent atmosphere measurements avoiding over-fitting. The improvement is based on the high resolution and sensitivity as well as the large spatial coverage of the radar data.

In particular, DInSAR data provide indirect measurements of pressure, temperature and humidity which are projected into SAR geometry and mapped into delay measurements physically related to refractivity. For this reason, the ensemble members can be assessed regarding their likelihood of occurrence. Instead of the straightforward best-fitting ensemble member, the weighted ensemble mean provides the final atmosphere hindcast.

For n ensemble members $F = \{f_1, \ldots, f_n\}$,

$$\mathrm{WEM}(F) = \sum_{i\in\{1,\ldots,n\}} a_i f_i \tag{1}$$

the weighted ensemble mean (**WEM**) with weights (likelihoods) $a_i \in \mathbb{R}_+$ and $\sum_{i\in\{1,\ldots,n\}} a_i = 1$ equals the expected value. In addition, the mass conservation can be relaxed to $\sum_{i\in\{1,\ldots,n\}} a_i \approx 1$ (R. Bamler, personal communication 4 May 2015). As a consequence, the estimated prediction can be improved in case of biased (i.e. physically incorrect) solutions.

The objective of the actual work is to present a framework which produces synergy between ensemble weather predictions and DInSAR measurements. It means both benefit from each other.

2. Methods

The APS (ϕ'_a) is composed of a hydrostatic term corresponding to (refractivity N_h) and a wet term corresponding to (refractivity N_w). Both are influenced by temperature (T). The hydrostatic term is additionally influenced by total pressure (P) while the wet term is influenced by water vapour (e). Based on physics, the range distance deviation is defined by

$$\phi'_a = 10^{-6} \int_{\vec{\boldsymbol{p}}_{(i,j)}}^{\vec{\boldsymbol{s}}} N(\vec{\boldsymbol{v}})\mathrm{d}\vec{\boldsymbol{v}} \tag{2}$$

where

$$N = \underbrace{K_1 \frac{P}{T}}_{N_h} + \underbrace{K_2 \frac{e}{T} + K_3 \frac{e}{T^2}}_{N_w}. \tag{3}$$

$\vec{\boldsymbol{p}}_{(i,j)}$ is the three dimensional location on Earth of the actual DInSAR pixel and $\vec{\boldsymbol{s}}$ is the position of the SAR-satellite. Eq. (3) models the refractivity (N) and the coefficients (K_1, K_2, K_3) are provided by Rüeger (2002). Practically, for every pixel of the SAR-image, integration through the predicted three dimensional atmospheric state produces an APS (ϕ'_a) candidate. A differential interferogram is composed of two SAR acquisitions. Of course, the corresponding APSs are needed for both acquisition times (τ_1, τ_2). From ensemble members and corresponding delays for both dates, candidates of APSs are computed ($\phi'_a(\tau_1, \cdot), \phi'_a(\tau_2, \cdot)$). A convex optimisation computes a least norm fit of the NWP data matrix **A** with respect to the DInSAR observation ($\phi_l(\tau_1, \tau_2)$) with $r \times c$ pixels:

$$\text{minimise}: \ ||r_k||_2 \tag{4}$$

subject to:

$$r_k = \left(\mathbf{A}a - \hat{\phi}_l(\tau_1, \tau_2)\right)_k \text{ for } k \in \{1, \ldots, rc\} \tag{5}$$

$$\sum_{k=1}^{n_{\tau_1}} \boldsymbol{a}_k = 1, \tag{6}$$

$$\sum_{k=n_{\tau_1}+1}^{n_{\tau_1}+n_{\tau_2}} -\boldsymbol{a}_k = 1, \tag{7}$$

$$\sum_{k=1}^{rc} A_{k,i} = 0 \text{ for } i \in \{1, \ldots, n_{\tau_1} + n_{\tau_2}\}, \tag{8}$$

$$\sum_{k=1}^{rc} \left(\hat{\phi}_l(\tau_1, \tau_2)\right)_k = 0. \tag{9}$$

where n_{τ_1}, n_{τ_2} are the counts of ensemble candidates. The last two constraints cope with the unknown interferometric phase offset. Practically, coefficients (a_i) of best-fitting linear combination are interpreted as likelihoods. In doing so, the WEM equals the expectation ($\mathrm{E}\{\cdot\}$) definition in a stochastic meaning. Therefore, the WEM equals the centre point of all predictions, such that the expected quadratic error is minimal.

2.1. Model of atmospheric phase screen approximation and algorithm

The starting point is an absolute DInSAR phase $\phi : \mathbb{N} \mapsto \mathbb{R}^{r\times c}$ at acquisition time τ with r rows and c columns (see Kampes, 2006):

$$\phi(\tau) = \phi_a(\tau) + \phi_d(\tau) + \phi_n(\tau) \tag{10}$$

ϕ_a, ϕ_d and $\phi_n : \mathbb{N} \mapsto \mathbb{R}^{r\times c}$ are the phase delays caused by the atmosphere, the deformation and noise, respectively.

An interferometric phase $\phi_l : \mathbb{N}^2 \mapsto \mathbb{R}^{r\times c}$ is defined by:

$$\phi_l(\tau_1, \tau_2) = \phi(\tau_1) - \phi(\tau_2) + \mathbf{O} \tag{11}$$

where **O** is a matrix (image) modelling the unknown interferometric phase offset. We assume that the atmosphere effect is statistically dominant compared to the deformation and the noise. Let $\phi'_a(\tau, k) : \mathbb{N}^2 \mapsto \mathbb{R}^{r\times c}$ be the k'th predicted APS candidate of a single SAR acquisition. Similar to the weighted ensemble mean, the corresponding APS candidates are weighted to approximate the SAR acquisition's atmosphere $\phi_a(\tau)$.

$$\phi(\tau) \approx \overbrace{\left(\sum_{k=1}^{n} a_\tau(k)\phi'_a(\tau, k)\right)}^{\approx\phi_a(\tau)} \tag{12}$$

where $0 \leqslant a_\tau(k) \leqslant 1$, $\sum a_\tau(k) = 1$ and without loss of generality $\phi'_a(\cdot,\cdot)$ are linearly independent.

Now, the observed DInSAR phase is approximated by

$$\phi_I(\tau_1,\tau_2) - \mathbf{O} \approx \tag{13}$$

$$\approx \sum_{k=1}^{n_{\tau_1}} a_{\tau_1}(k)\phi'_a(\tau_1,k) - \sum_{k=1}^{n_{\tau_2}} a_{\tau_2}(k)\phi'_a(\tau_2,k). \tag{14}$$

The constraints $a_\tau(k) \in \mathbb{R}_+$ and $\sum_{k\in\{1,\dots,n\}} a_\tau(k) = 1$ allow interpretation of the coefficients a_{τ_1} and a_{τ_2} as likelihoods. In the following, we derive a matrix notation to compute these likelihoods efficiently and finally obtain the SAR acquisitions atmosphere.

Approximation (14) is rewritten to a constrained $(a_{\tau_1}(k), a_{\tau_2}(k) \geqslant 0)$ set of linear equations. It consists of:

$$r_{(i,j)} = \left(\sum_{k=1}^{n_{\tau_1}} a_{\tau_1}(k)\phi'_a(\tau_1,k) + \sum_{k=1}^{n_{\tau_1}} -a_{\tau_2}(k)\phi'_a(\tau_2,k) + \mathbf{O} - \phi_I(\tau_1,\tau_2) \right)_{(i,j)}. \tag{15}$$

where $r_{(i,j)}$ is the residual of range-azimuth position (pixel) i,j. We denote $\hat{\boldsymbol{M}}$ the column vector representation of any matrix $\mathbf{M}$. For practical reasons, this set of equations is minimised over the sum of $r^2_{(i,j)}$ which is written as

$$\operatorname{argmin}_{\boldsymbol{a}} ||\mathbf{A}\boldsymbol{a} - \hat{\phi}_I(\tau_1,\tau_2)||_2^2, \text{ where} \tag{16}$$

$$\boldsymbol{a_i} = \begin{cases} a_{\tau_1}(i), & \text{if } 1 \leqslant i \leqslant n_{\tau_1} \\ -a_{\tau_2}(i - n_{\tau_1}), & \text{if } n_{\tau_1}+1 \leqslant i \leqslant n_{\tau_1}+n_{\tau_2} \\ \text{arbitrary}, & \text{for } i = n_{\tau_1}+n_{\tau_2}+1 \end{cases} \tag{17}$$

$$\mathbf{A}_{,i} = \begin{cases} \hat{\phi}'_a(\tau_1,i), & \text{if } 1 \leqslant i \leqslant n_{\tau_1} \\ \hat{\phi}'_a(\tau_2,i-n_{\tau_1}), & \text{if } n_{\tau_1}+1 \leqslant i \leqslant n_{\tau_1}+n_{\tau_2} \\ 1, & \text{for } i = n_{\tau_1}+n_{\tau_2}+1 \end{cases} \tag{18}$$

$$\sum_{k=1}^{n_{\tau_1}} \boldsymbol{a}_k = 1, \tag{19}$$

$$\sum_{k=n_{\tau_1}+1}^{n_{\tau_1}+n_{\tau_2}} -\boldsymbol{a}_k = 1, \tag{20}$$

$$0 \leqslant \boldsymbol{a}_k \leqslant 1, k \in \{1,\dots,n_{\tau_1}\} \text{ and } -1 \leqslant \boldsymbol{a}_k \leqslant 0, k \in \{n_{\tau_1}+1,\dots,n_{\tau_2}\}. \tag{21}$$

Negative entries in $\boldsymbol{a}$ follow from the first minus in Eq. (15) and $\boldsymbol{a}_{n_{\tau_1}+n_{\tau_2}+1}$ corresponds to $\hat{\boldsymbol{O}}$.

This matrix description realised by Algorithm 1 allows us to apply a practically available solver e.g. *lsqlin* from MATLAB to obtain the solution.

2.2. Algorithm extension

The actual algorithm does not separate deformation and atmosphere. As a consequence, NWP ensemble members which also fit the deformation signal are favoured and the corresponding motion signal leaks into the atmosphere. Of course, it results in a biased APS and an underestimated deformation. Practically, this effect can be mitigated and even eliminated. First, the mitigation is achieved by using short temporally-separated SAR acquisitions. A small deformation phase results, which is in practice below the precision of the NWP. We would like to illustrate this situation with numbers. The typical deformation in PSI is up to 20 mm per year. For ERS and a time separation of 35 days, the interferometric deformation signal is about 0.4 rad. In contrast, the NWP hydrostatic component has a standard deviation of $\frac{1}{\cos 21^\circ}$ 2.5 mm (for $\sigma_T = 1$ K, $\sigma_P = 1$ h Pa) (see Adam, 2013) respective $\frac{1}{\cos 21^\circ}$ 0.56 rad which deteriorates considering also the wet component. Following this argument, sensors with a short repeat cycle e.g. Sentinel-1 are predestined for this technique. Second, the bias can be eliminated for all SAR-acquisitions except for two. For this purpose, the algorithm needs to be updated for a stack of SAR acquisitions. We define

$$\phi_{Id}(\tau_1,\tau_2) = T(\tau_1,\tau_2)\boldsymbol{\phi}_d = \phi_d(\tau_1) - \phi_d(\tau_2) \tag{22}$$

where $T : \mathbb{N}^2 \mapsto \mathbb{R}$ is a known temporal dependent function which models the deformation $\boldsymbol{\phi}_d \in \mathbb{R}^{r\times c}$. A linear deformation model is often sufficient, but a seasonal deformation is straightforward to implement as well.

$\phi_I(\tau_1,\tau_2)$ is now divided into a deformation related part and the corresponding residuum

$$\phi_I(\tau_1,\tau_2) = \phi_{Ir}(\tau_1,\tau_2) + T(\tau_1,\tau_2)\boldsymbol{\phi}_d. \tag{23}$$

Eq. (16) is rewritten to

$$\operatorname{argmin}_{\boldsymbol{a}} ||\mathbf{A}\boldsymbol{a} - \hat{\phi}_{Ir}(\tau_1,\tau_2) - T(\tau_1,\tau_2)\hat{\boldsymbol{\phi}}_d||_2^2 \tag{24}$$

while constraints (17)–(21) are satisfied. A second interferogram between times τ_2 and τ_3 $(\tau_1 < \tau_2 < \tau_3)$ is introduced and a second optimisation is done simultaneously. Now, the optimisation of the questioned NWP ensemble is supported by two DInSAR data sets with alternating deformation signals. This second optimisation is denoted by

$$\operatorname{argmin}_{\boldsymbol{a}'} ||\mathbf{A}'\boldsymbol{a}' - \hat{\phi}_{Ir}(\tau_3,\tau_2) - T(\tau_3,\tau_2)\hat{\boldsymbol{\phi}}_d||_2^2. \tag{25}$$

Of course, the coefficients of $\boldsymbol{a}$ and $\boldsymbol{a}'$ related to time τ_2 need to be equal in describing the same atmosphere. This is formalised by

$$\operatorname{argmin}_{\boldsymbol{a}''} ||\mathbf{A}''\boldsymbol{a}'' - \phi_{Pr} - \boldsymbol{\phi}_{Pd}||_2^2 \tag{26}$$

where

$$\mathbf{A}'' = \begin{pmatrix} \mathbf{A} & \mathbf{0} \\ \mathbf{0} & \mathbf{A}' \end{pmatrix}, \tag{27}$$

$$\phi_{Pr} = \begin{pmatrix} \hat{\phi}_{Ir}(\tau_1,\tau_2) \\ \hat{\phi}_{Ir}(\tau_3,\tau_2) \end{pmatrix}, \tag{28}$$

$$\phi_{Pd} = \begin{pmatrix} T(\tau_1,\tau_2)\hat{\boldsymbol{\phi}}_d \\ T(\tau_3,\tau_2)\hat{\boldsymbol{\phi}}_d \end{pmatrix}, \tag{29}$$

$$\boldsymbol{a}'' = \begin{pmatrix} \boldsymbol{a} \\ \boldsymbol{a}' \end{pmatrix} \text{ and that for each pair} \tag{30}$$

$$a_i \in \boldsymbol{a}, a_j \in \boldsymbol{a}' \text{ which are related to the ensemble index } k\left(\hat{\phi}'_a(\tau_2,k)\right) \tag{31}$$

$$a_i - a_j = 0. \tag{32}$$

Deformation $\hat{\boldsymbol{\phi}}_d$ affects the coefficients which are related to time τ_2 equally, if $T(\tau_1,\tau_2) = -T(\tau_3,\tau_2)$. Consequently, these coefficients are no longer biased by the deformation. Corresponding proof is presented below. An equal deformation signal is obtained if the interferograms are multiplied with $|T(\tau_i,\tau_j)|^{-1}$. Therefore, the APSs are also amplified by this factor, such that constraints (19) and (20) have to be modified. For the interferogram between times τ_1 and τ_2 substitute 1 by $|T(\tau_1,\tau_2)|^{-1}$ and for interferogram between times τ_3 and τ_2 by $|T(\tau_3,\tau_2)|^{-1}$. Also, constraint (32) is modified to $|T(\tau_1,\tau_2)|^{-1}a_i - |T(\tau_3,\tau_2)|^{-1}a_j = 0$.

For a series of interferograms between times $\tau_1 < \cdots < \tau_n$, this extension is applied recursively. Now, only coefficients related to τ_1 and τ_n are affected by the deformation. To mitigate the influence of the first and last scene's deformation and atmosphere effects, the interferograms should be generated with short time separation and from winter scenes.

Proof. Rows of $\mathbf{A}''$ are assumed to be linearly independent, which is almost surely the case. A squared regular matrix $\mathbf{C}$ exists then, such that rows of $\mathbf{A}''\mathbf{C}$ are orthogonal. The Gram-Schmidt process calculates such a linear transformation. Starting with the vector-space related to τ_1 and τ_3 guaranties, that $\mathbf{C}^{-1}\boldsymbol{a}'' = (\boldsymbol{a}_1''^T, \boldsymbol{a}_2''^T)^T$ and $\mathbf{A}''\mathbf{C} = (\mathbf{A}_1'', \mathbf{A}_2'')$ can be reordered such that all coefficients which are related to time τ_2 are exclusively within $\boldsymbol{a}_2''$. The optimisation (26) can be divided into two independent parts with respect to $\boldsymbol{a}_1''$ and $\boldsymbol{a}_2''$ because of the linear transformation into an orthogonal space (due to $\mathbf{C}$).

The starting point is

$$\operatorname{argmin}_{\boldsymbol{a}_2''} ||\mathbf{A}_2''\boldsymbol{a}_2'' - \phi_{\mathrm{Pr}} + \phi_{\mathrm{Pd}}||_2^2 \tag{33}$$

since the proof is exclusively related to coefficients within $\boldsymbol{a}_2''$. Only coefficients which are related to time τ_2 are within $\boldsymbol{a}_2''$, such that $\mathbf{A}_2''$ can be reordered again to

$$\mathbf{A}_2'' = \begin{pmatrix} \mathbf{B} & \mathbf{0} \\ \mathbf{0} & \mathbf{B} \end{pmatrix} \tag{34}$$

while $\boldsymbol{a}_2''^T = (\boldsymbol{b}^T, \boldsymbol{b}^T)$ according to constraint (32). For better readability, we substitute $\hat{\phi}_{\mathrm{I_r}}(\tau_1, \tau_2) = R_1$, $\hat{\phi}_{\mathrm{I_r}}(\tau_3, \tau_2) = R_2$ and $T(\tau_1, \tau_2)\hat{\boldsymbol{\phi}}_{\mathrm{d}} = -T(\tau_3, \tau_2)\hat{\boldsymbol{\phi}}_{\mathrm{d}} = D$ and the count of rows of B is now denoted by n. Optimisation (33) is rewritten to

$$\operatorname{argmin}_{\boldsymbol{b}} \sum_k^n \left(\mathbf{B}_{(k,\cdot)}\boldsymbol{b} - R_{1_k} + D_k\right)^2 + \left(\mathbf{B}_{(k,\cdot)}\boldsymbol{b} - R_{2_k} - D_k\right)^2 \tag{35}$$

$$= \operatorname{argmin}_{\boldsymbol{b}} \sum_k^n \mathbf{B}_{(k,\cdot)}\boldsymbol{b}(2\mathbf{B}_{(k,\cdot)}\boldsymbol{b} - 2R_{1_k} - 2R_{2_k}) + \tag{36}$$

$$+ D_k(2D_k - 2R_{1_k} + 2R_{2_k}) + R_{1_k}^2 + R_{2_k}^2 \tag{37}$$

$$= \operatorname{argmin}_{\boldsymbol{b}} \sum_k^n \mathbf{B}_{(k,\cdot)}\boldsymbol{b}\left(2\mathbf{B}_{(k,\cdot)}\boldsymbol{b} - 2R_{1_k} - 2R_{2_k}\right) \tag{38}$$

which does not depend on $D = T(\cdot,\cdot)\hat{\phi}_{\mathrm{d}}$. □

3. Results

The presented method is applied to a real interferogram from the well-known Netherlands DInSAR test site for a practical demonstration and verification (see Figs. 1 and 2). Hanssen et al. (1999) state that DInSARs are beneficial for forecasting and atmospheric studies. One of the presented scenarios is repeated. First, we show the mitigation of the APS in an interferogram (see Fig. 3). Second, the two estimated weighted ensemble mean weather hindcasts are compared with independent sea level pressure data.

In the following, we describe the experiment setup. All NWPs were computed by the weather research and forecast model (**WRF** version 3.5) with ten different micro physics options (mp_physics $\in \{0, \ldots, 9\}$). A complete description of WRF and the mentioned options can be found in Skamarock et al. (2008). Dates were chosen with respect to the DInSAR acquisition times on 3rd and 4th October 1995. The corresponding interferogram was derived from 1-day revisit acquisitions at 21:41 UTC of ERS 1/2 tandem mission. Three domains with 13,500 m, 2700 m and 900 m resolution were used while each domain has about 200×200 grid cells. Initialisation time was 12:00 UTC and the current state for the finest domain was written out every 10 min. A four hour time window (±2 h) of possible delay is chosen, such that in both cases 250 possible APSs were generated. The initialisation data are ERA-interim ECMWF with 0.75° resolution (see European Centre for Medium-Range Weather Forecasts, 2009).

In doing so, we demonstrate that this technique is useful for APS correction as well as for forecasting skills and atmospheric studies as Hanssen et al. (1999) stated.

3.1. APS mitigation in DInSAR by ensembles hindcasts

The test site is characterised by dominant atmosphere effects. Topography has a negligible effect on the interferometric phase due to a baseline of 388 m and the very flat terrain. We first demonstrate the APS compensation assuming the interferometric phase corresponds completely to the atmosphere signal (see Fig. 2). The short time separation of one day supports this assumption. Second, we show that the presented algorithm is robust with respect to typical geophysical deformation signals (see Fig. 4). For this reason, we simulate a deformation phase in the real interferogram. The criteria to measure the mitigation and to compare the improvement is the RMSE of the atmosphere compensated interferogram (e.g. the residual of Figs. 3(b) and 5(b)). Table 1 provides the measured residuals from six estimation scenarios on the two experiments.

The first scenario represents the uncompensated APS according to the assumption that the DInSAR residual phase corresponds to the atmosphere only. The second scenario (blind NWP) is the straightforward NWP with *mp_physics* option 8 at acquisition time since it is the well-tested parametrisation of WRF (see chapter 5 in the WRF user guide from Wang et al., 2013). The third scenario corresponds to the unweighted ensemble mean. The fourth scenario is an improvement because it selects from a set of hindcasts the best-fitting one. In practice, the proposed algorithm provides this solution by selecting the ensemble members with the largest coefficients. The fifth scenario provides the weighted ensemble mean (see Figs. 3 and 5). The last two scenarios demonstrate further estimations with relaxations of the constraints (19) and (20) which allow better fits, assuming biased hindcasts.

3.1.1. Without deformation

This experiment is summarised by the second column of Table 1. In this table, large numbers correspond to uncompensated APS. First of all, each NWP-based mitigation scenario improves the differential interferogram. Straightforward mitigation techniques, i.e. the unweighted ensemble and the blind NWP, improve the DInSAR phase by 11–13%. Interestingly, the blind NWP outperforms the unweighted ensemble mean. This result confirms the well-tested physics parameters and supports the assumption of some non-physical solutions in the ensemble. The mitigation performance improves using techniques jointly using DInSAR and NWP data (synergy). It is a result of data-adaptive estimation and of the increased amount of additional data and information. In numbers, the single best-fitting estimation improves the DInSAR phase by ca. 27% and the weighted ensemble estimations (see Fig. 3) even by ca. 45%. In summary, the proposed ensemble technique improves the APS mitigation by a factor of four compared to the conventional NWP mitigation and by a factor of two compared to the single best-fitting technique.

Table 2 provides the estimated coefficients for this test case. For the 3rd October, many small coefficients are estimated whereas for the 4th October, three dominant coefficients are estimated. It results from the fact that the later acquisition is affected by a squall line (which is caused by a cold front, see Hanssen et al., 1999)

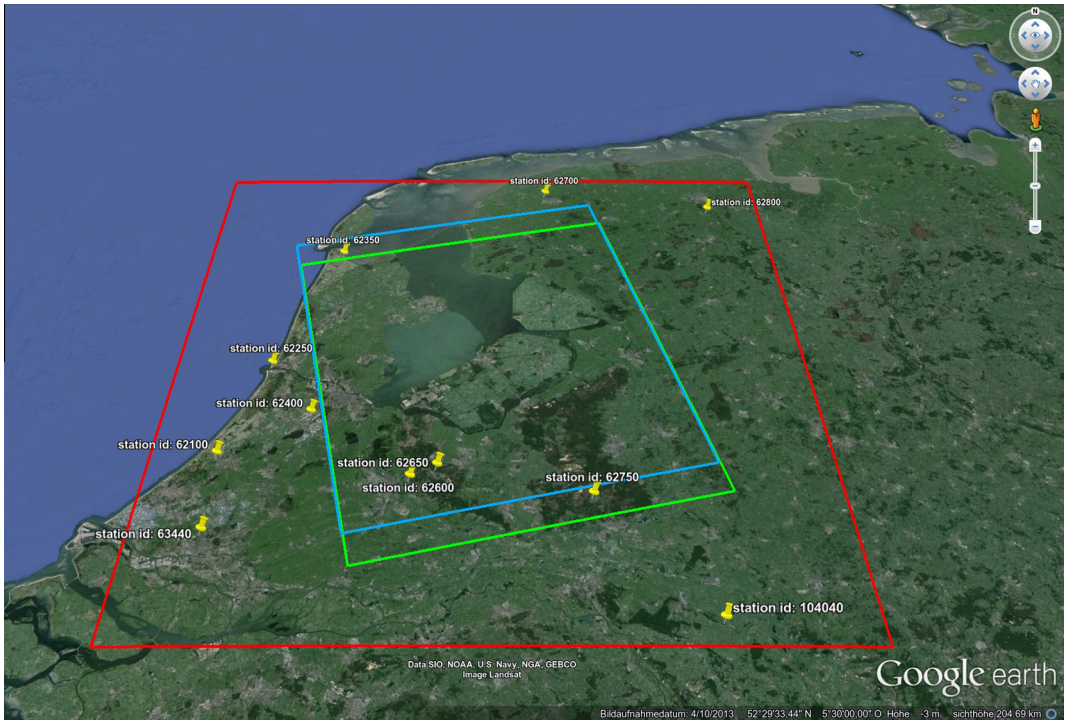

Fig. 1. Illustration of test site. The outer rectangle is the finest domain of NWP while the inner rectangles illustrate the SAR coverage of the acquisitions on 3rd and 4th October 1995. Weather stations are illustrated by yellow pins. The DInSAR image corresponds to the intersection of inner rectangles.

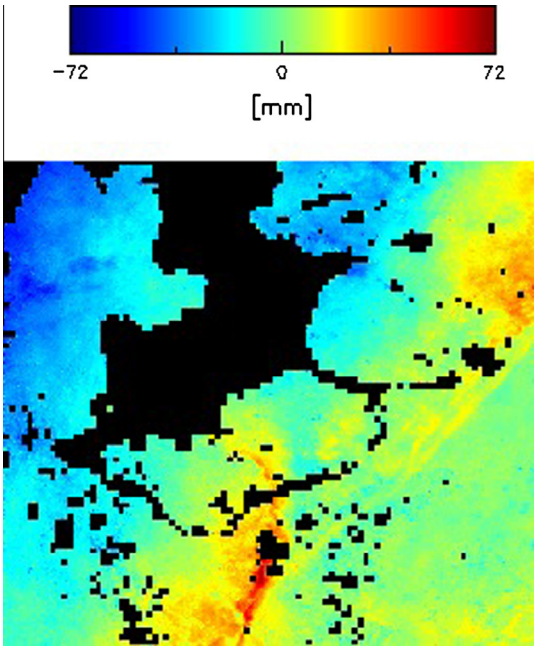

Fig. 2. DInSAR of 3rd and 4th October 1995 at 21:41 UTC is shown (see Hanssen et al., 1999 for a detailed description).

which is a significant and large feature of the atmospheric state to fit.

3.1.2. With deformation

In order to demonstrate the robustness of this approach with respect to typical deformation, a subsidence signal is simulated into the differential interferogram. Using these data, the test case above is repeated. In column three of Table 1, the APS mitigation improvement is always in the same order as the undisturbed experiment. A deformation interferes with the optimal solution since a best fit was computed including the deformation. The root mean squared error increases only insignificantly, illustrated by the difference between the two rows of Table 1. For completeness, Table 2 provides the estimated coefficients within the "disturbed" column. Practically, only very small changes of these coefficients can be observed. The experiment data are visualised in Fig. 4.

The robustness of the estimation in the presence of deformation improves, if exclusively the hydrostatic component is considered. Evidently, the hydrostatic component has a different spatial characteristic (much smoother) compared to the deformation signal. In contrast, the characteristic of the wet component is of higher spatial frequency and is consequently closer to the spatial frequency of the deformation. We demonstrate this robustness with an illustrative experiment. The starting points are the original $\phi_{\mathrm{I}}^{\mathrm{O}}$ and with a deformation modified differential interferogram $\phi_{\mathrm{I}}^{\mathrm{M}}$. The APS is estimated for both $(\phi_{\mathrm{a}}'^{\mathrm{M}}, \phi_{\mathrm{a}}'^{\mathrm{O}})$ based on the total delay and on only the hydrostatic delay. We assume the differential phase is composed of deformation and atmosphere

$$\phi_{\mathrm{I}} = \phi_{\mathrm{d}} + \phi_{\mathrm{a}} \tag{39}$$

and the original interferogram is free of deformation. The simulated deformation can now be recovered by

$$\phi_{\mathrm{d}} = \left(\phi_{\mathrm{I}}^{\mathrm{M}} - \phi_{\mathrm{a}}'^{\mathrm{M}}\right) - \left(\phi_{\mathrm{I}}^{\mathrm{O}} - \phi_{\mathrm{a}}'^{\mathrm{O}}\right) \tag{40}$$

in cases where the deformation does not infer with the estimation $(\phi_{\mathrm{a}}'^{\mathrm{O}} = \phi_{\mathrm{a}}'^{\mathrm{M}})$. The similarity with respect to the simulated deformation describes the robustness of the estimation. We provide the recovered deformation phase ϕ_{d} for the estimation based on the total delay (see Fig. 6(a)) and the estimation based on the hydrostatic delay (see Fig. 6(b)). A straightforward visual inspection demonstrates the clear advantage with respect to robustness of using only the hydrostatic delay.

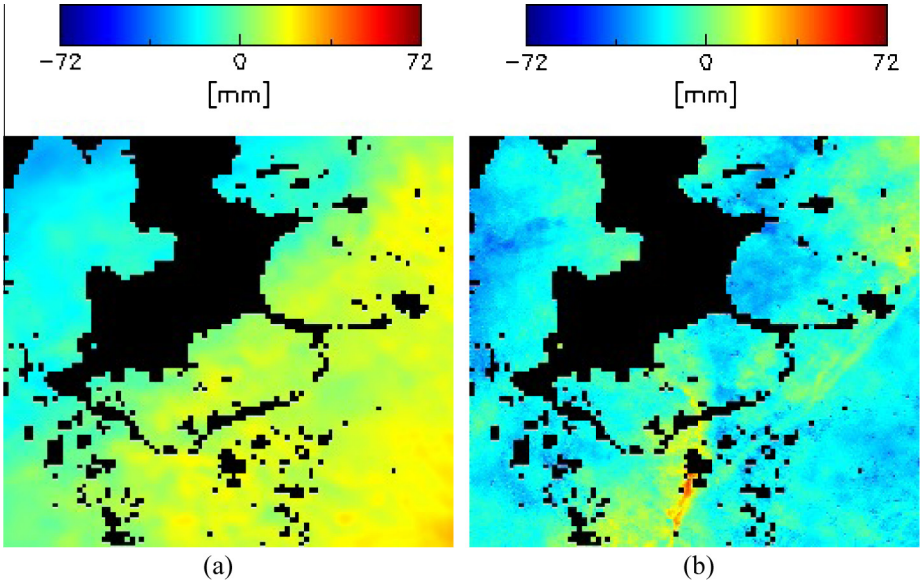

Fig. 3. (a) Estimated APS using the total delay. (b) Correspondingly corrected DInSAR from Fig. 2.

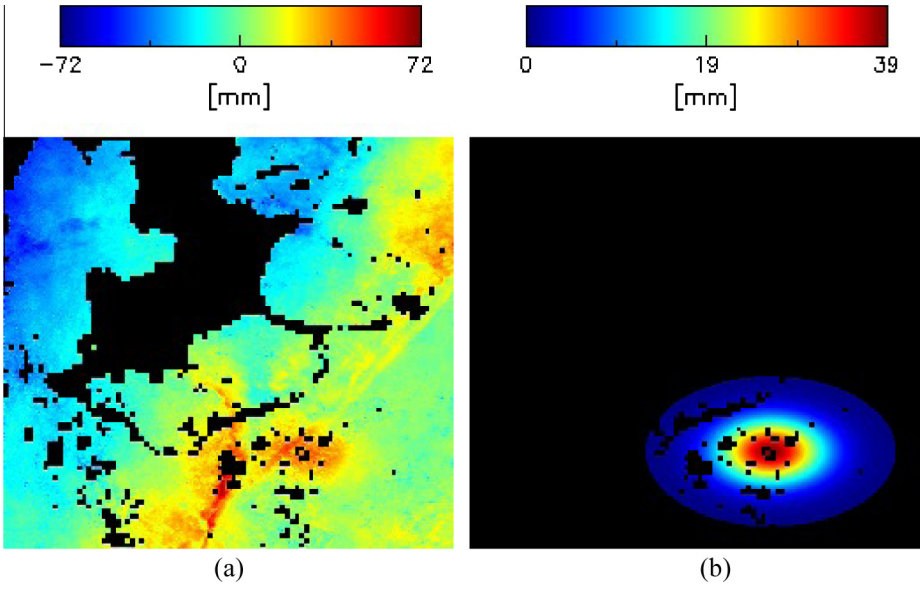

Fig. 4. (a) Modified DInSAR of Fig. 2. (b) Simulated deformation.

3.2. Differential synthetic aperture radar interferogram correction improves ensemble hindcasts

In this test case, the two estimated weighted ensemble mean weather hindcasts are compared with independent sea level pressure data and averaged ensemble members. At the time of acquisition, 11 meteorological stations are available ($n = 11$, see Fig. 1) in this test site.

Surface pressure and temperature data are publicly accessible (from the Integrated Surface Hourly Database) and have a temporal resolution down to one hour. The time of SAR acquisitions is 21:41, so the delay relative to the measurements is, in our case, only 19 min. This is small enough to validate the precision.

The estimation needs to be based on the hydrostatic component for the following reasons. The most variability of the APS is within the wet term and therefore dominates the hydrostatic term (Hanssen et al., 1999). If the total delay of the ensemble members is fitted, the likelihoods of the ensemble members with respect to water vapour are estimated. By using only the hydrostatic term,

Table 1
Root mean squared error in [mm] of non-compensated APS.

	Real interferogram	Real interferogram + deformation
Uncompensated APS	18.01	
Blind NWP	15.72	
Unweighted ensemble	16.04	
Single best-fitting	13.09	13.09
Weighted ensemble	9.83	10.09
Weighted ensemble (relaxed to ≈ 1)	9.04	9.36
Weighted ensemble (without constraint)	8.34	8.85

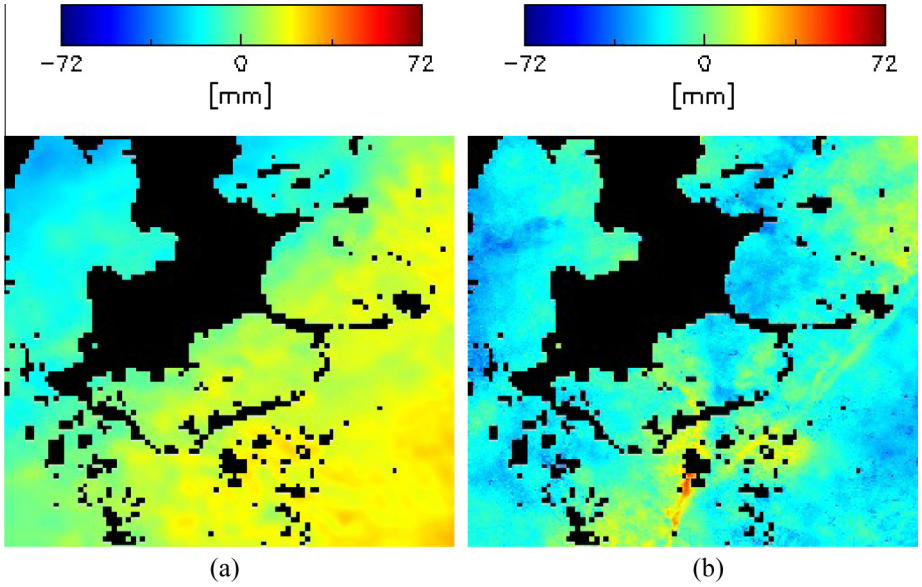

Fig. 5. (a) Estimated APS using the total delay and the modified DInSAR from Fig. 4. (b) Correspondingly corrected DInSAR from Fig. 4.

Table 2
Computed fitting coefficients of argmin (16) with respect to DInSAR (original) and to DInSAR with deformation (disturbed).

	Original	Disturbed	*mp_physics*	Acquisition time
October 3	0.16	0.17	2	22:30
	0.13	0.17	2	22:40
	0.06	0	3	23:40
	0.09	0.01	5	23:30
	0.15	0.11	7	22:20
	0.09	0.12	7	23:10
	0.06	0	7	23:00
	0	0.04	7	23:30
	0.08	0.10	8	22:20
	0.08	0.04	9	23:10
	0.07	0.11	9	23:20
	0.03	0.13	9	23:30
October 4	0.52	0.46	0	23:40
	0.21	0.28	1	19:40
	0.21	0.22	1	21:00
	0.06	0.04	8	19:40

the likelihoods of the ensemble members with respect to pressure are derived. This is a valid assumption since the hydrostatic delay can be approximated just by the surface pressure (see Davis et al., 1985).

The criteria to measure the improvement is the Forecast Skill (see Murphy, 1988). The mean squared error of two forecasts $f = \{f_1, f_2\}$ is defined by

$$\mathrm{MSE}(f,x) = \frac{1}{2n}\sum_{i=1}^{2}\sum_{j=1}^{n}(f_i(j) - x_i(j))^2 \tag{41}$$

where $f_i(j)$ and $x_i(j)$ are the forecast and the observation at date i is at position j. The skill factor is defined by

$$\mathrm{SS}(f,r,x) = 1 - \frac{\mathrm{MSE}(f)}{\mathrm{MSE}(r)} \tag{42}$$

where $r = \{r_1, r_2\}$ are the reference forecasts. If no additional data are available, the average of the ensemble members are used in practice. As a consequence, the reference forecast is the unweighted mean

$$r_i = \frac{1}{10}\sum_{j=0}^{9} e_j \tag{43}$$

where e_j is the ensemble member with *mp_physics* option j at date i. f_i is the WEM at date i where the weights equal the fitting coefficients. In our test case, the skill factor is

$$\mathrm{SS}(f,r,x) = 0.29 \tag{44}$$

which means, that the derived estimate has 29% lower MSE as the reference.

Temperature-induced delay variations can be observed and are straightforward to identify, as Hanssen et al. (1999) has already mentioned (see diagonal pattern of Fig. 2). A rapid change of temperature induces a rapid change in pressure through diabatic heating (compare Figs. 7 and 8). Therefore, the cold front effect within the DInSAR is supportive for finding the best prediction with respect to pressure.

3.3. Application test case with Sentinel-1 data

A test case with Sentinel-1 data at Mexico City demonstrates the practical benefit of the introduced technique on complex topography and modern data. This city is characterised by subsidence areas of 25 mm/month because of continuous water extraction (see Chaussard et al., 2014). This known strong continuous subsidence allows us to validate the introduced method. Therefore, two interferograms are considered and the respective APSs are compensated similar to the Netherland test case using the extended algorithm. The acquisition date of the master scene is the 02-12-2014 and the dates of the slave scenes are 27-10-2014 and 26-12-2014. Similarly to PSI, linear deformation estimations are derived by the linear regression technique. Therefore, interferograms with uncompensated and compensated APSs are assessed and the results are compared in Fig. 9. Now, the advantage of the introduced technique is illustrated with three arguments. First, the Mexico City subsidence, highlighted by the black circle in Fig. 9(b), of 25 mm/month is better estimated in 9(b) compared to 9(a). Second, the vertical stratification effect, i.e. the APS correlation with height is now completely mitigated (highlighted

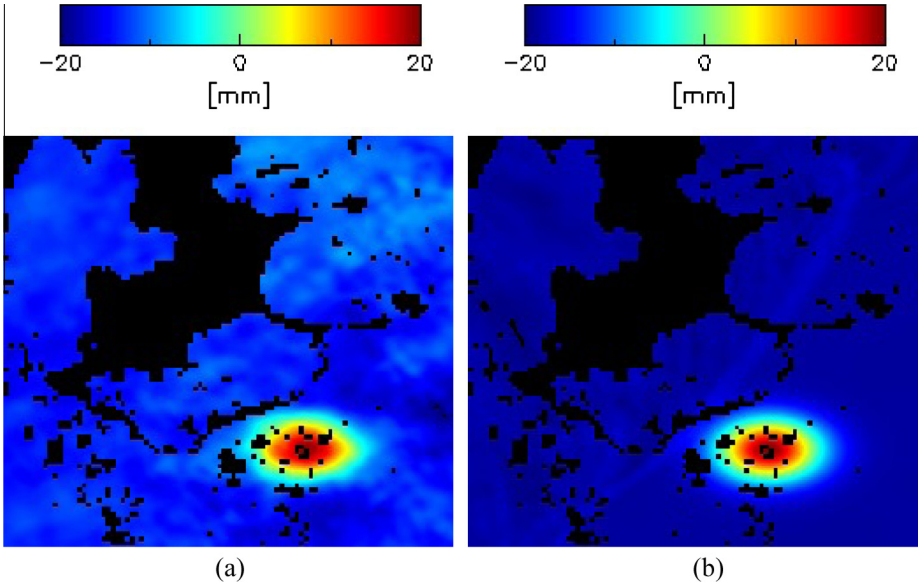

Fig. 6. (a) Recovered deformation phase ϕ_d using (a) total delay and (b) hydrostatic delay.

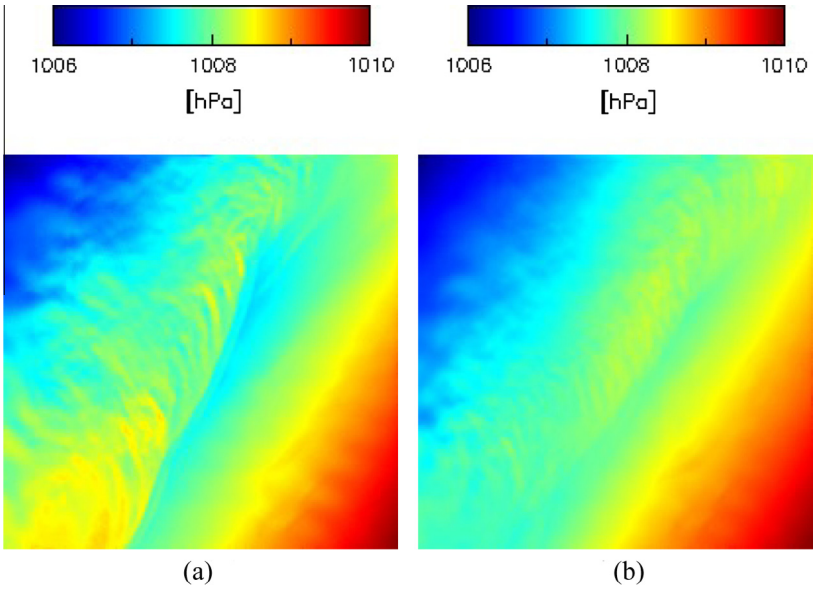

Fig. 7. Surface pressure prediction at October 4th of (a) WEM (b) unweighted ensemble at 21:40 UTC.

in Fig. 9(a)). Third, the standard deviations of the differential interferograms as a measure for uncompensated line of sight effects (i.e. the digital elevation model update, the deformation and the APSs) are reduced and provided in Table 3. The proposed method reduces the APS caused standard deviations by about 33 and 46 percent.

4. Discussion

In this section, our results are generalised and the impact of the algorithm on the PSI technique is illustrated. The basic estimation of PSI can be traced back to a time series analysis. In principle, it is a frequency estimation problem. For the error propagation assessment, a linear regression of interferometric phase versus acquisition time t_i can be used instead of a frequency estimation (see Rocca, 2004). The precision of the velocity estimation σ_d depends on the number of acquisitions (N) and the interferometric phase noise σ_a:

$$\sigma_d = \sigma_a \sqrt{\frac{1}{N \operatorname{Var}(t_i)}}. \tag{45}$$

Assuming persistent scatterers with a high signal to clutter ratio are used, the APS dominates the interferometric phase noise and the atmosphere mitigation directly reduces σ_a. Our algorithm reduces the APS standard deviation by a factor of 0.55. Assuming a test case with an estimation precision of 1 mm per year, the estimation precision improves using compensated differential interferograms to about 0.55 mm per year. In cases where the processing objective is to achieve a precision of 1 mm per year, the number of scenes can be reduced by a factor of 0.55^2 i.e. by about 70%. Of course, it directly maps into a data cost reduction of 70%.

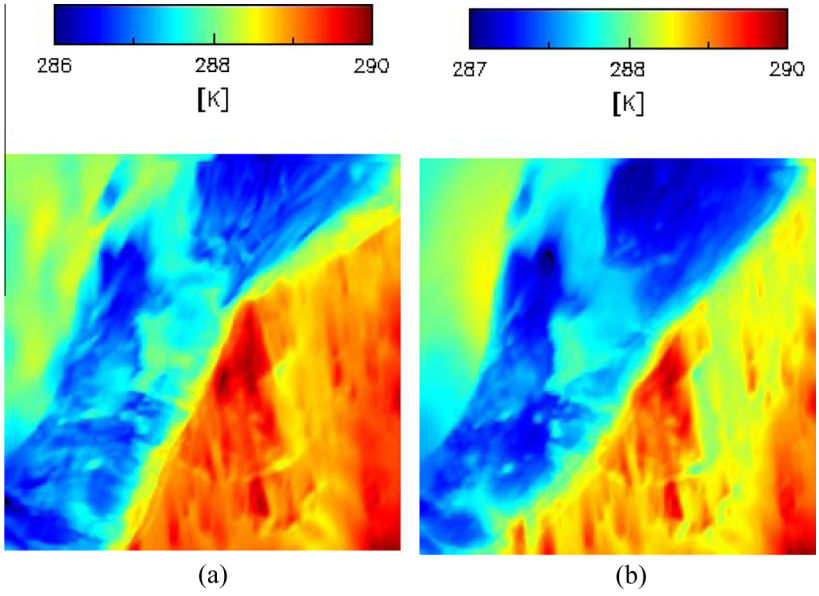

Fig. 8. Temperature prediction at October 4th of (a) WEM (b) unweighted ensemble at 21:40 UTC.

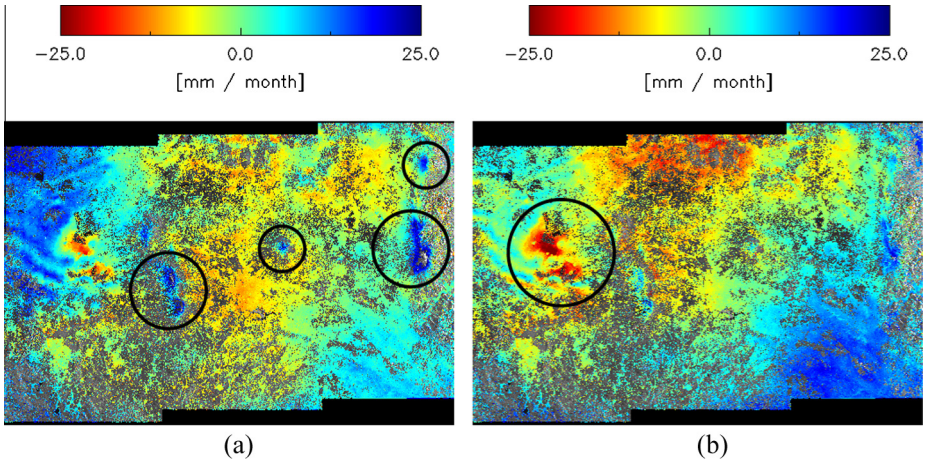

Fig. 9. Linear deformation estimations of (a) uncompensated interferograms and (b) compensated interferograms.

Table 3
Standard deviation [mm] of interferograms.

Slave dates	Uncompensated APS	Compensated APS
2015-10-27	16.35	10.93
2015-12-26	21.95	11.72

5. Conclusion

The objective of this paper is to show the synergy between ensemble weather predictions and differential interferometric atmosphere correction. The basis is the joined analysis of two independent data sets (DInSAR and ECMWF) which both include the information of the atmospheres refractivity. A practical framework is presented which enables useful applications in differential interferometry and NWP. The differential interferometry and time series techniques benefit by a reduction of the APS by 45%. This achievement can be transformed into improved precision or into a data cost reduction. The presented technique is robust with respect to deformations. The NWP benefits from improved precision which is demonstrated by the atmosphere pressure. The test case shows 29% improvement.

The framework applications are demonstrated using the Netherlands test site. Due to the existence of only nearly flat terrain, the atmosphere mitigation in DInSAR is based on the wet effect and the respective timing correction. In contrast, in the presence of strong topography, the atmosphere stratification is the dominant effect and is typically straightforward to mitigate.

Acknowledgement

For the interferometric processing, DLR's GENESIS system has been used. The authors thank the development team for their support. The WRF has been developed by the National Centre for Atmospheric Research (NCAR) and its partners. The ECMWF ERA-interim data for driving the regional model simulations are provided by the European Centre for Medium-Range Weather Forecasts (ECMWF). Additionally, we thank Richard Bamler, Thomas Trautmann, Michael Eineder and Moritz Fischer for the constructive suggestions which greatly helped to improve this paper.

Appendix A. Algorithm in pseudo-code notation

Algorithm 1. Algorithm to estimate the APS from the WEM and the expected NWP

Data: DInSAR image $\phi_I(\tau_1, \tau_2)$ and initialisation data for predictions
Result: Most likely prediction and most likely APS of DInSAR
/* build up matrix for least squares fit and WEM: */
$\mathbf{A}, \mathbf{F}$:= empty matrix variable
forall $\tau_i \in \{\tau_1, \tau_2\}$ **do**
  forall $k \leqslant n_{\tau_i}$ **do**
    $f_k(\tau_i)$:= predict for acquisition time τ_i the k'th ensemble member
    $\phi'_a(\tau_i, k)$:= compute corresponding APS of ensemble member $f_k(\tau_i)$
    $\hat{\phi}'_a(\tau_i, k)$:= convert matrix $\phi'_a(\tau_i, k)$ to a column vector
    $\mathbf{A} := \left(\mathbf{A}, \hat{\phi}'_a(\tau_i, k)\right)$
    $\hat{f}_k(\tau_i)$:= convert $f_k(\tau_i)$ to a column vector
    $\mathbf{F} := \left(\mathbf{F}, \hat{f}_k(\tau_i)\right)$
  end
end
$\mathbf{A} := \begin{pmatrix} \mathbf{A}, & \begin{matrix} 1 \\ \vdots \\ 1 \end{matrix} \end{pmatrix}$
$\hat{\phi}_I(\tau_1, \tau_2)$:= convert matrix $\phi_I(\tau_1, \tau_2)$ to a column vector
/* solve least squares problem with bounds and restrictions: */
$a := \operatorname{argmin}_{\boldsymbol{a}} ||\mathbf{A}\boldsymbol{a} - \hat{\phi}_I(\tau_1, \tau_2)||_2^2$ where constraints (19)–(21) are satisfied
/* final steps for vector represented results: */
Expected prediction (stochastic meaning) at time τ_1:
$\mathrm{WEM}(F) = \sum_{i \in \{1,\ldots,n_{\tau_1}\}} a_i \mathbf{F}_{\cdot,i}$
Expected prediction (stochastic meaning) at time τ_2:
$\mathrm{WEM}(F) = \sum_{i \in \{n_{\tau_1}+1,\ldots,n_{\tau_1}+n_{\tau_2}\}} - a_i \mathbf{F}_{\cdot,i}$
Most plausible APS of initial DInSAR: $\mathbf{A}\boldsymbol{a}$

References

Adam, N., 2013. Algorithmic PSI Improvement in Mountainous Areas by Atmosphere Mitigation. Technical Report. DLR.

Chaussard, E., Wdowinski, S., Cabral-Cano, E., Amelung, F., 2014. Land subsidence in central Mexico detected by {ALOS} InSAR time-series. Remote Sens. Environ. 140, 94–106. http://dx.doi.org/10.1016/j.rse.2013.08.038, <http://www.sciencedirect.com/science/article/pii/S0034425713002964>.

Davis, J.L., Herring, T.A., Shapiro, I.I., Rogers, A.E.E., Elgered, G., 1985. Geodesy by radio interferometry: effects of atmospheric modeling errors on estimates of baseline length. Radio Sci. 20, 1593–1607.

Epstein, E.S., 1969. Stochastic dynamic prediction1. Tellus 21, 739–759. http://dx.doi.org/10.1111/j.2153-3490.1969.tb00483.x.

European Centre for Medium-Range Weather Forecasts, 2009. European Centre for Medium-Range Weather Forecasts (ECMWF) Re-Analysis Interim (ERA-Interim) Model data. <http://catalogue.ceda.ac.uk/uuid/00f58d1d7b6c8f38993e77c79e72da92>.

Ferretti, A., Prati, C., Rocca, F., 2001. Permanent scatterers in SAR interferometry. IEEE Trans. Geosci. Remote Sens. 39, 8–20.

Hanssen, R.F., Weckwerth, T.M., Zebker, H.A., Klees, R., 1999. High-resolution water vapor mapping from interferometric radar measurements. Science 283, 1297–1299.

Holley, R., Wadge, G., Zhu, M. (Eds.), 2007. New insights into the nature and effects of the water vapour field on InSAR measurements over Etna. In: FRINGE.

Jung, J., Kim, D., Park, S.E., 2014. Correction of atmospheric phase screen in time series InSAR using WRF model for monitoring volcanic activities. IEEE Trans. Geosci. Remote Sens. 52, 2678–2689. http://dx.doi.org/10.1109/TGRS.2013.2264532.

Kampes, B., 2006. Radar Interferometry: Persistent Scatterer Technique. Remote Sensing and Digital Image Processing. Springer.

Liu, S., Mika, A., Gong, W., Hanssen, R., Meyer, F., Morton, D., Webley, P., 2011. The role of weather models in mitigation of tropospheric delay for SAR interferometry. In: 2011 IEEE International Geoscience and Remote Sensing Symposium (IGARSS), pp. 2562–2565. 10.1109/IGARSS.2011.6049735.

Murphy, A.H., 1988. Skill scores based on the mean square error and their relationships to the correlation coefficient. Mon. Weather Rev. 116, 2417. http://dx.doi.org/10.1175/1520-0493(1988)116<2417:SSBOTM>2.0.CO;2.

Nico, G., Tome, R., Catalao, J., Miranda, P., 2011. On the use of the WRF model to mitigate tropospheric phase delay effects in SAR interferograms. IEEE Trans. Geosci. Remote Sens. 49, 4970–4976. http://dx.doi.org/10.1109/TGRS.2011.2157511.

Perissin, D., Rocca, F., Pierdicca, M., Pichelli, E., Cimini, D., Venuti, G., Rommen, B., 2011. Mitigation of atmospheric delay in InSAR: the ESA metawave project. In: 2011 IEEE International Geoscience and Remote Sensing Symposium (IGARSS), pp. 2558–2561. http://dx.doi.org/10.1109/IGARSS.2011.6049734.

Pichelli, E., Ferretti, R., Cimini, D., Panegrossi, G., Perissin, D., Pierdicca, N., Rocca, F., Rommen, B., 2015. InSAR water vapor data assimilation into mesoscale model MM5: technique and pilot study. IEEE J. Sel. Top. Appl. Earth Observ. Remote Sens. PP, 1–17. http://dx.doi.org/10.1109/JSTARS.2014.2357685.

Pierdicca, N., Rocca, F., Basili, P., Bonafoni, S., Carlesimo, G., Cimini, D., Ciotti, P., Ferretti, R., Marzano, F., Mattioli, V., Montopoli, M., Notarpietro, R., Perissin, D., Pichelli, E., Rommen, B., Venuti, G., 2011. Synergic use of EO, NWP and ground based measurements for the mitigation of vapour artefacts in SAR interferometry. In: 2011 IEEE International Geoscience and Remote Sensing Symposium (IGARSS), pp. 2566–2569. http://dx.doi.org/10.1109/IGARSS.2011.6049765.

Rocca, F., 2004. Diameters of the orbital tubes in long-term interferometric SAR surveys. IEEE Geosci. Remote Sens. Lett. 1, 224–227, <http://ieeexplore.ieee.org/xpls/abs_all.jsp?arnumber=1315637>.

Rüeger, J.M., 2002. Refractive index formulae for radio waves.

Skamarock, W.C., Klemp, J.B., Dudhia, J., Gill, D.O., Barker, M., Duda, K.G., Huang, X.Y., Wang, W., Powers, J.G., 2008. A description of the Advanced Research WRF Version 3. Technical Report. National Center for Atmospheric Research.

Smith, E., Weintraub, S. (Eds.), 1953. The Constants in the Equation for Atmospheric Refractive Index at Radio Frequencies.

Wang, W., Bruyre, C., Duda, M., Dudhia, J., Gill, D., Kavulich, M., Keene, K., Lin, H.C., Michalakes, J., Rizvi, S., Zhang, X., 2013. ARW Version 3 Modeling System Users Guide January 2014. Technical Report. National Center for Atmospheric Research.